Zaytsev et al., http://www.jcb.org/cgi/content/full/jcb.201312107/DC1

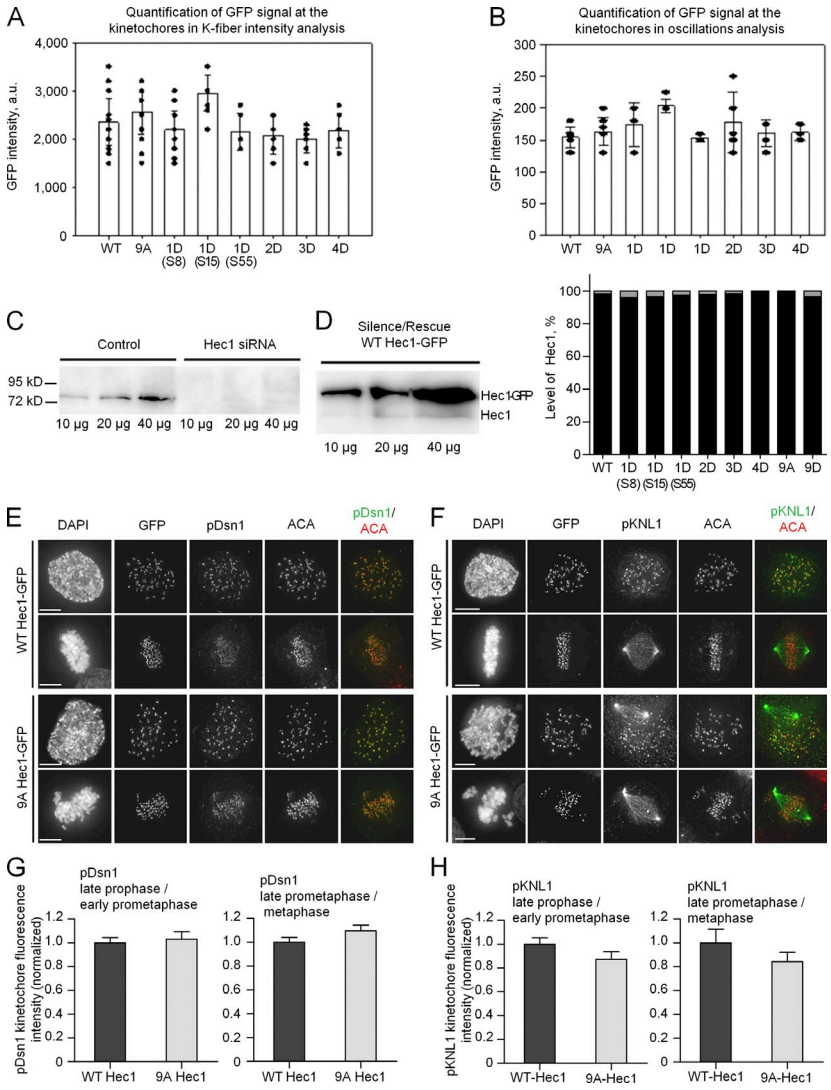

Figure S1. **Experimental analysis of phosphoregulation of the KMT interface.** (A) Quantification of Hec1-GFP fusion protein levels at kinetochores in fixed PtK1 cells. Data for each group represent at least eight kinetochores from at least six cells. Bars indicate the mean values for all cells; circles represent mean data for kinetochores from individual cells. Error bars are SDs. Cells measured here correspond to those measured in Fig. 3. (B) Quantification of Hec1-GFP fusion protein levels at kinetochores in live PtK1 cells. Data represent at least six kinetochores per cell from at least seven cells. Bars indicate the mean values for all cells; circles represent mean data for kinetochores from individual cells. Error bars are SDs. Cells measured here correspond to those measured in Fig. 2. Data in E and F show that protein levels of different Hec1-GFP proteins were roughly similar, and they exhibited no trend. (C) Quantification of Hec1 depletion. Western blots of mock-transfected and Hec1 siRNA–transfected cell lysates stained with antibodies to Hec1 are shown. Hec1 siRNA transfection results in a >95% decrease in total protein levels. By immunofluorescence staining, kinetochore levels of Hec1 are reduced in siRNA-transfected cells to ∼8% of control level (not depicted). (D) Analysis of endogenous and exogenous Hec1 in cells treated with Hec1 siRNA and rescued with various Hec1-GFP fusions. (left) Western blot stained with Hec1 antibodies showing endogenous Hec1 (bottom band) and exogenously expressed WT Hec1-GFP (top band). The amount of lysate loaded in each lane is indicated. (right) Quantification of Western blot results for all Hec1-GFP fusions used in the study. In the graph, black represents the level of exogenously expressed Hec1; gray represents endogenous Hec1. On average, the level of endogenous Hec1 was ∼2% of exogenous (with a range between 0.3 and 4%). (E) Images of immunostained HeLa cells with antibodies to phospho-Dsn1 (pDsn1), a phosphoregulatable kinetochore component. Top images for both WT Hec1-GFP and 9A Hec1-GFP show late prophase/early prometaphase cells; the bottom images show late prometaphase/metaphase cells. Chromosomes are stained with DAPI; kinetochores are stained with anticentromere antibodies (ACA). (F) Images of immunostained HeLa cells with antibodies to phospho-KNL1 (pKNL1), a phosphoregulatable kinetochore component. For WT Hec1-GFP and 9A Hec1-GFP, the top images show late prophase/early prometaphase cells; the bottom images show late prometaphase/metaphase cells. (G) Quantification of pDsn1 kinetochore fluorescence intensities. Values are normalized to WT Hec1. Error bars represent SEMs. Number of cells analyzed for each condition $n \geq 8$; number of kinetochores analyzed $n \geq 103$. We additionally quantified pDsn1 kinetochore levels in early prometaphase cells expressing 9D Hec1-GFP and found no significant difference when compared with levels at kinetochores in early prometaphase cells expressing WT Hec1-GFP (not depicted). HeLa cells were used for the experiments shown in E–H because pDsn1 and pKNL1 are not highly cross-reactive in PtK1 cells. (H) Quantification of pKNL1 kinetochore fluorescence intensities. Values are normalized to WT Hec1. Error bars represent SEMs. Number of cells analyzed for each condition $n \geq 5$; number of kinetochores analyzed $n \geq 51$. The phosphorylation of both Dsn1 and Knl1 is statistically similar in cells expressing WT Hec1 and nonphosphorylatable Hec1. These data demonstrate that prevention of Hec1 phosphorylation by expression of 9A Hec1-GFP does not alter phosphorylation levels of the kinetochore proteins Dsn1 and KNL1 in either prometaphase or metaphase. a.u., arbitrary unit. Bars, 10 µm.

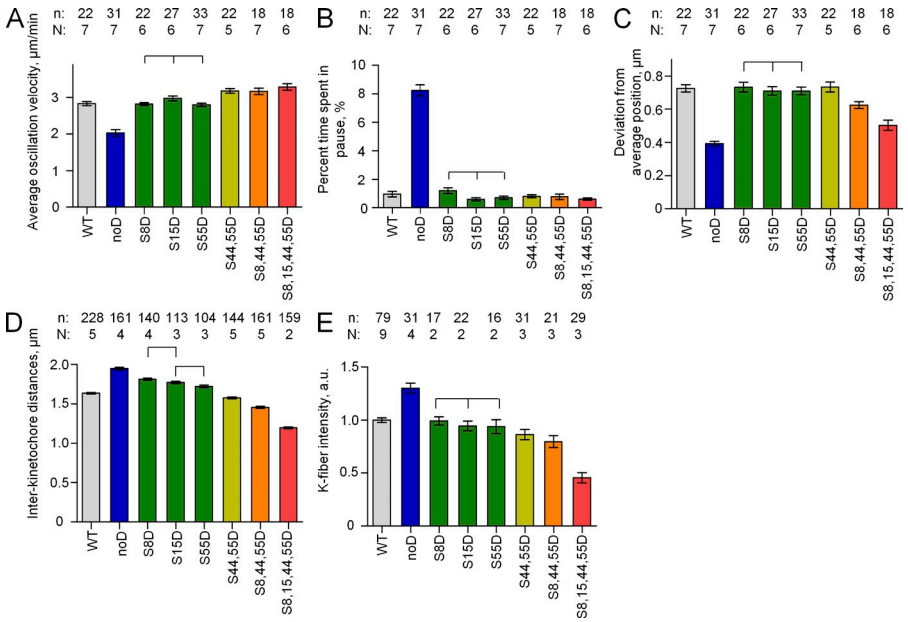

Figure S2. **Statistics for cell experiments with different numbers and locations of phosphomimetic substitutions.** (A–E) These data are the same as in Fig. 2 (C–E), but cells expressing different 1D Hec1 mutants are compared, and the number of examined cells, n, and the number of independent experiments, N, are provided. The exact positions of phosphomimetic substitutions are indicated below each bar. Brackets indicate datasets that are not statistically different ($P > 0.05$). Error bars are SEMs. (A) Mean velocity of kinetochore movement along the spindle axis in metaphase cells expressing Hec1 with different numbers of phosphomimetic substitutions. (B) Percentage of time spent with no motion for two sequential frames during chromosome oscillations in metaphase cells expressing Hec1 mutants with different phosphomimetic substitutions. (C) Deviation from average position, a measure of chromosome oscillation amplitude, in metaphase cells expressing Hec1 mutants with different phosphomimetic substitutions. The difference between 1D, 2D, 3D, and WT was not significant. This result can be explained by the fact that cells with either hyper- or hypostable kinetochore–MT attachments exhibit decreased oscillation amplitudes. Thus, as we move from a 9A situation (hyperstable attachments) to increasing numbers of D substitutions in the A background (increasingly hypostable attachments), we observe that cells expressing any of the D mutants exhibit oscillation amplitudes that are, on average, lower than those measured in control cells. (D) Interkinetochore distances in metaphase cells expressing Hec1 mutants with different phosphomimetic substitutions. (E) K-fiber intensities in metaphase cells expressing different Hec1 mutants. Results are normalized to data for WT Hec1. a.u., arbitrary unit.

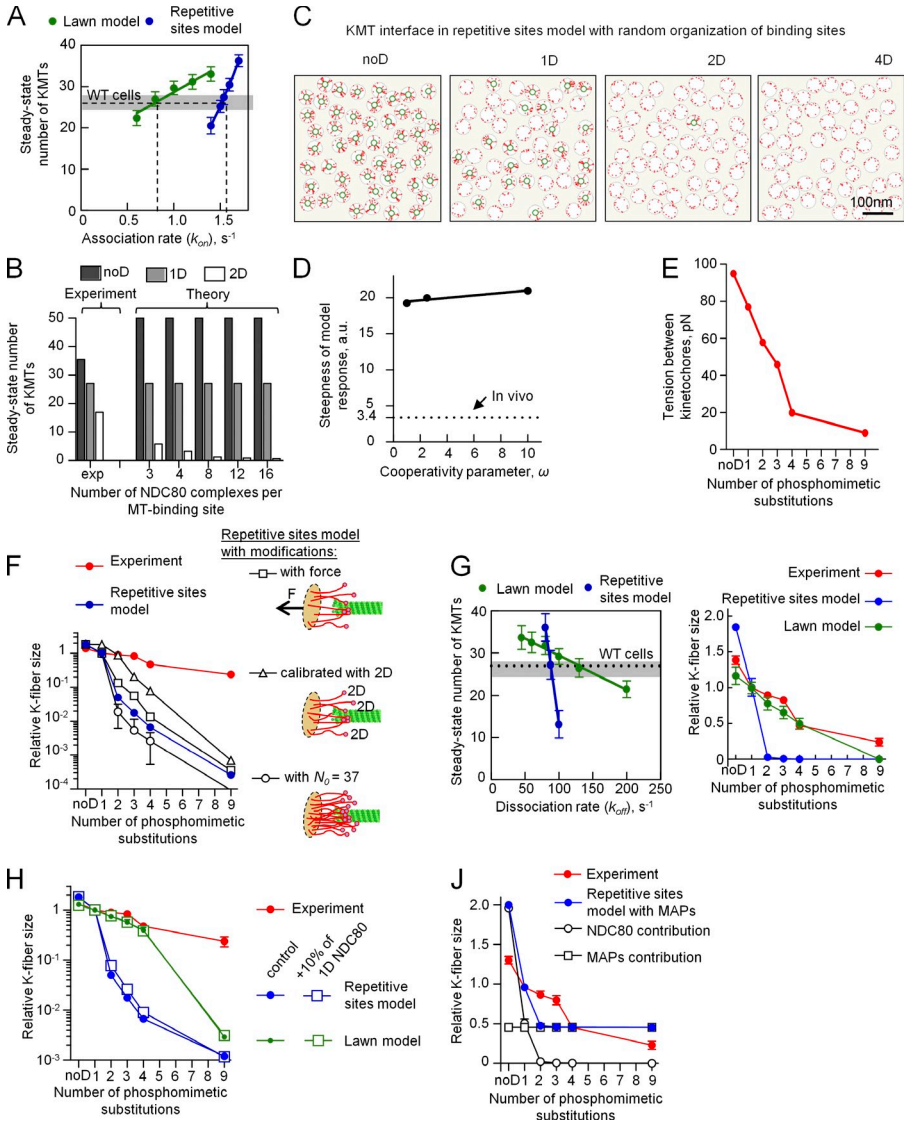

Figure S3. **Mathematical modeling of the KMT interface.** (A) Calibration procedure for the two models. Horizontal gray area depicts the range for the number of KMTs observed in metaphase PtK1 cells. The mean value (27) is indicated with a horizontal dashed line (based on McEwen et al., 1997). Symbols are means with SDs based on a simulation time of 6 h for each mode for each point on the curve; colored lines are linear fits. Vertical dashed lines correspond to the association rates at which the models reproduce the experimental number of KMTs. This fitting procedure yielded k_{on} = 0.8 s^{-1} for the dynamic lawn model and k_{on} = 1.52 s^{-1} for the repetitive sites model (Table 1). These values were used for all model calculations. (B) The steady-state number of KMTs for three different phosphorylated forms of the NDC80 complex (noD, 1D, and 2D) in the repetitive sites model with a different number of NDC80 complexes per site. Fewer NDC80 complexes per binding site results in a smaller amplification, and the dependency becomes less steep. However, even for three NDC80 complexes per site, the model provides a poor match to the experimental data (left bars). (C) These images were prepared analogously to Fig. 4 E, but calculations were performed with the repetitive sites model in which the positions of the sites were random. All other model parameters, including the number of NDC80 complexes per site, were left unchanged. The steepness of phosphoregulation is clearly visible. (D) Steepness of the response to phosphorylation in the repetitive sites model for different values of the cooperativity parameter. The dashed line indicates a steepness of 3.4 (relative value) measured with the experimental curve in Fig. 4 D. See Materials and methods section Sensitivity analysis of the repetitive sites model for a description of how steepness was determined. a.u., arbitrary unit. (E) Estimated tension between sister kinetochores in cells with different Hec1 phosphomutants. See Materials and methods section Sensitivity analysis of the repetitive sites model for details. (F) Predicted K-fiber size in different variants of the repetitive sites model. The original model (blue symbols; data same as in Fig. 4 D but plotted on semilog scale) was modified (a) to incorporate tension-sensitive dissociation of NDC80 complexes from MTs (squares; see legend on the right from the graph), (b) to calibrate the model differently by using molecular constants for 2D NDC80 complexes, and (c) to increase the number of NDC80 complexes per binding site to N_0 = 37. None of these modifications enabled this model to match the experimental curve. (G) Alternative model calibration strategy that uses a fixed value of k_{on} = 50 s^{-1}. The steady-state number of KMTs was calculated to identify the values of k_{off} = 88 s^{-1} for the repetitive sites model and k_{off} = 130 s^{-1} for the lawn model, which provide the physiological number of KMTs (shown with a dotted line). The graph on the right shows predicted phosphoregulation curves for these two models. These results are highly similar to those obtained with the main calibration strategy (Fig. 4 D), illustrating that the difference between the models does not depend on this procedure. See Materials and methods Model calibration section for details. (H) Modeling results for kinetochores containing 10% endogenous NDC80 complexes and 90% exogenously expressed NDC80 complexes, indicated on the horizontal axis. Because K-fiber size is calculated for a steady-state situation, the endogenous NDC80 complexes were assumed to have the molecular characteristics of 1D NDC80 complexes. Theoretical control (no endogenous NDC80 complexes) and experimental data are from Fig. 4 D. These data show that the model predictions do not depend on the presence of a small fraction of endogenous NDC80 complexes. In our experiments, <4% of endogenous Hec1 was left after siRNA-mediated depletion (Fig. S1 D). (J) Theoretical prediction of K-fiber size in the repetitive sites model containing MAPs with constant MT binding affinity. Experimental data are the same as in Fig. 4 D. Even the best possible fit (with minimal sum of squared residuals) provides a poor match to the experimental data. See Materials and methods section Modeling the kinetochore with a mixture of NDC80 complexes and generic MAP molecules for details. Error bars are SEMs.

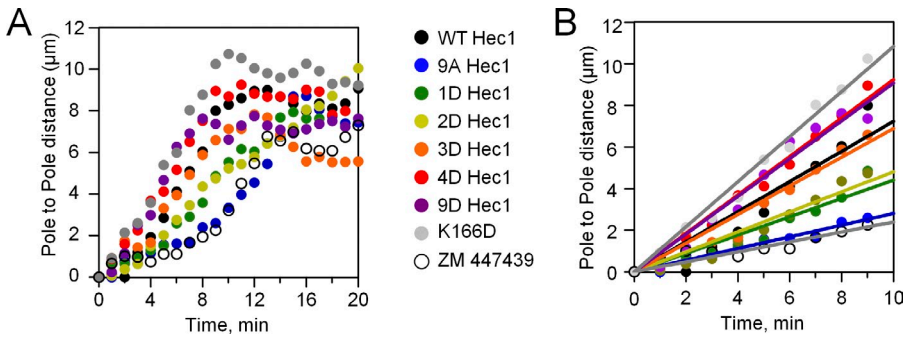

Figure S4. **Analysis of spindle pole separation in live cells.** (A) Plots show pole-to-pole distance versus time for cells released from a monastrol arrest. Data are from cells depleted of endogenous Hec1 and rescued with the indicated Hec1 mutants. Also shown on the graph are data from cells treated with an Aurora B kinase inhibitor (ZM447439) and cells expressing a Hec1 calponin homology domain mutant (K166D), which inhibits the formation of stable KMTs in vivo (Sundin et al., 2011) and MT binding in vitro (Ciferri et al., 2008). In most cells, the distance between the poles increases almost linearly and then reaches a plateau. (B) Initial time segment for curves shown in A. Experimental data are shown with symbols (see legend in A). Lines are linear fits. Spindle pole separation rates were determined from the slope of these curves.

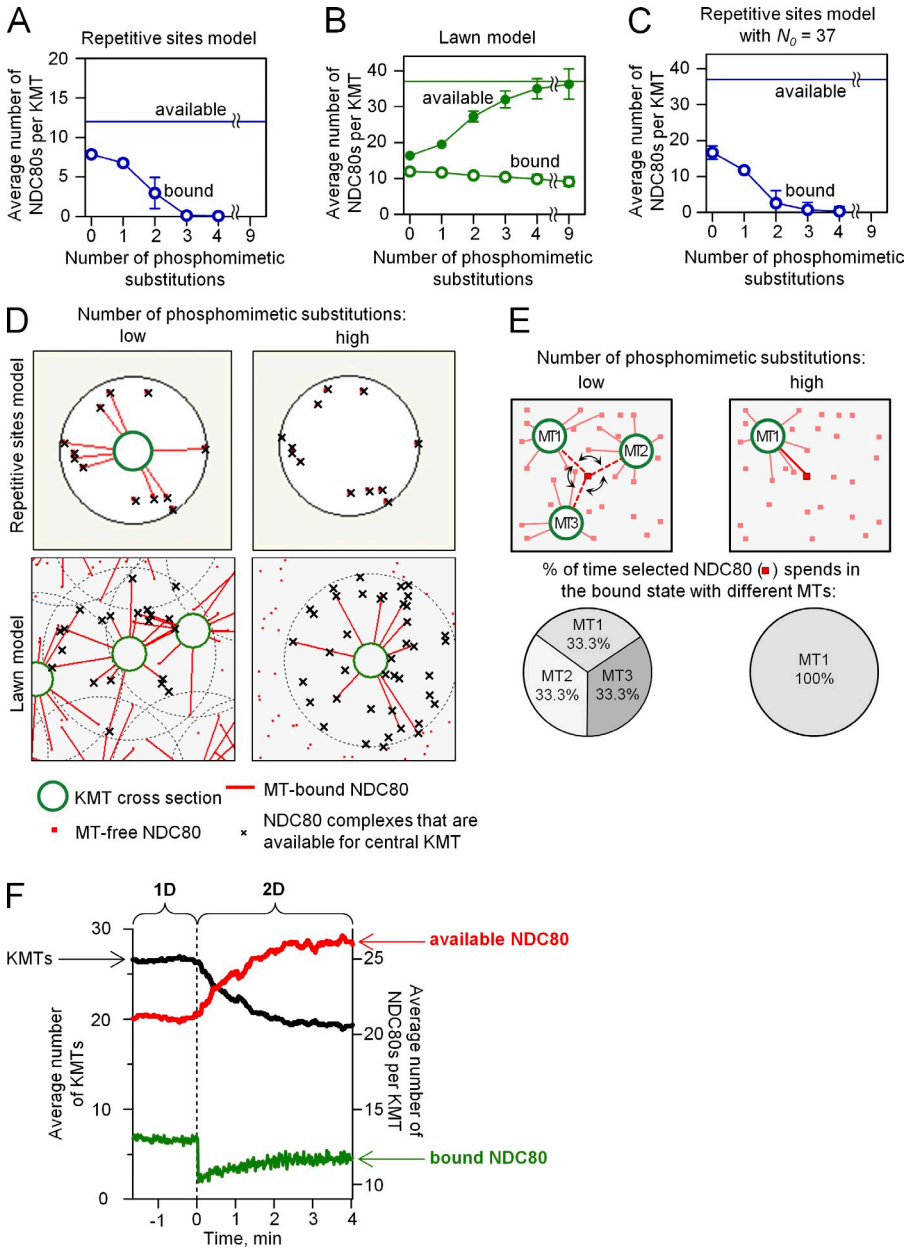

Figure S5. **Molecular rules of KMT binding in the repetitive sites model versus the lawn model.** (A) Mean number of complexes that are bound to one KMT at steady state, as calculated for kinetochores with different NDC80 complexes in the repetitive sites model. In this model, the number of NDC80 complexes that are potentially available for binding one MT is the same for all interfaces and is simply the number of NDC80 complexes per one binding site, N_0 = 12 (Table 2). (B) Analogous plots as in A but for the lawn model. The maximal number of NDC80 complexes in the lawn interface that can reach one KMT is 37 (horizontal line; see Materials and methods section General description). This number is limited by the total number of NDC80 complexes per kinetochore (same as in the repetitive sites model), by the kinetochore size (same as in the repetitive sites model), and by the length of the NDC80 complex (60 nm; Table 2). As the number of phosphomimetic substitutions decreases, the individual NDC80–MT molecular bonds become stronger, so the number of attached KMTs increases. Although the total number of NDC80 complexes and their kinetochore densities do not change, when the KMT density is higher, the number of "available" NDC80 molecules per one KMT decreases because of their sharing by adjacent KMTs. Thus, the pool of available binders per KMT in the dynamic lawn model is variable, unlike in the repetitive sites model. Decrease in the number of available binders is compensated owing to mass action law by their stronger molecular affinity, explaining the relatively small change in the number of MT-bound complexes in different interfaces (open circles; compare with A). Likewise, the increase in the number of available complexes stabilizes KMT attachments, thereby counteracting the decrease in affinity of the single molecules. (C) These plots are analogous to those in A, but the data shown are for the repetitive sites model with N_0 = 37 NDC80 complexes per MT binding site. Increasing the number of NDC80 complexes per site increases the absolute number of MT-bound complexes for all phosphomutants, but it further increases the steepness of the phosphoregulation response (Fig. S3 F). (D) Illustration of the molecular interactions between kinetochore-associated NDC80 complexes and KMTs and their response to phosphoregulation. The number of NDC80 complexes that are available for binding the central KMT in each image remains constant in the repetitive sites model for all levels of NDC80 phosphorylation and does not depend on the number of attached MTs. However, the number of available NDC80 complexes increases in the lawn model with a decreasing number of KMTs, which become less stable when an NDC80 complex is phosphorylated and its dissociation rate increases. In both models, NDC80 complex phosphorylation weakens NDC80–MT affinity, but only in the dynamic lawn model does the loss of some KMTs free the NDC80 complexes to immediately become available for binding with the remaining KMTs. Sharing of NDC80 complexes by adjacent KMTs is a key factor that explains a graded response to phosphorylation in the lawn model (also see Video 3). (E) The schematic illustrates the dynamic reorganization of NDC80–MT interactions for different degrees of Hec1 phosphorylation. When Hec1 phosphorylation is low and there are more KMTs, the NDC80 complex in the center (red square) can potentially bind any of the shown three KMTs, so it is shared, as illustrated with the pie chart on the bottom. When Hec1 phosphorylation increases and there are fewer KMTs, the highlighted NDC80 complex can now bind only to the remaining MT1, thereby increasing stability of this MT. (F) Kinetics of the changes in the number of available and MT-bound NDC80 complexes in the lawn model in response to phosphorylation. Calculations were performed analogously to Video 3. Curves are averaged from n = 10 simulations. At time t = 0 min (vertical dotted line), the lawn interface was changed from 1D to 2D NDC80. Error bars are SEMs.

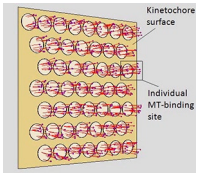

Video 1. **Kinetochore–MT interface in the repetitive sites model.** A planar square represents the kinetochore with predefined MT binding sites (circles), each containing 12 NDC80 complexes. One site can bind only one MT. The simulation starts with the kinetochore with no MTs, and then, MTs (shown as green cylinders) start occupying free sites. After ~20 min, the number of KMTs reaches the steady state with 27 ± 3 KMTs, corresponding to the metaphase K-fiber size in PtK1 cells. The results shown in this video were obtained using parameter values for 1D NDC80 (Table 1 and Table 2). The iteration time step for this and all other videos is 1 ms. The probabilistic nature of NDC80–MT interactions is depicted by fluctuations in the orientation of NDC80 complexes to emphasize the transient and highly dynamic nature of their binding/unbinding to KMTs. Total simulated time was 20 min, played at 15 fps.

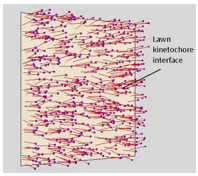

Video 2. **Kinetochore–MT interface in the dynamic lawn model.** This calculation was performed analogously to Video 1, using the same total number of NDC80 complexes and other model parameters (Table 2), but here, NDC80 complexes can bind to any MTs in their vicinity. As in Video 1, the number of KMTs increases gradually and reaches the steady state of 27 ± 3 KMTs, demonstrating that a good match to experimental data regarding K-fiber size and dynamics at metaphase can be obtained regardless of the overall design of the KMT interface. However, the rules of molecular interactions between NDC80 complexes and MTs play a critical role in defining how the interface responds to phosphorylation.

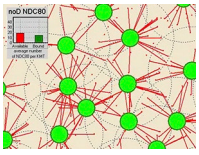

Video 3. **Phosphotuning of NDC80 molecules in the dynamic lawn leads to a smooth adjustment of K-fiber size.** Area of the kinetochore interface as in Video 2. MT-free NDC80 complexes are depicted with red dots, and they are shown with lines when they bind to MTs. Each MT can interact with multiple NDC80 complexes located within a circled area centered on this MT. As the number of KMTs increases, the black circles begin to overlap, and KMTs are forced to compete for NDC80 complexes, as evidenced from the decreasing number of complexes that are available, on average, for binding one KMT (red bar on the graph inset). The calculation starts with the interface composed of fully unphosphorylated NDC80 proteins, and steady state is reached with a K-fiber size of 34 ± 2 KMTs that turn over with a mean half-life of 16 ± 1 min; the mean number of available NDC80 complexes is 16 per KMT, of which, on average, 12 molecules are MT bound. NDC80 complex phosphorylation is then increased by gradually changing the dissociation rate of NDC80 complexes, as specified in Table 1, whereas all other parameters are kept constant. The video illustrates that the K-fiber size decreases smoothly. A lack of amplification of single molecule tuning is explained by the increasing pool of available NDC80 complexes at the kinetochores with fewer remaining KMTs, and the resulting stabilization of the number of MT-bound complexes (green bar on the graph inset). Total simulation time was 50 min, played at 15 fps.

References

Ciferri, C., S. Pasqualato, E. Screpanti, G. Varetti, S. Santaguida, G. Dos Reis, A. Maiolica, J. Polka, J.G. De Luca, P. De Wulf, et al. 2008. Implications for kinetochore-microtubule attachment from the structure of an engineered Ndc80 complex. *Cell*. 133:427–439. http://dx.doi.org/10.1016/j.cell.2008.03.020

McEwen, B.F., A.B. Heagle, G.O. Cassels, K.F. Buttle, and C.L. Rieder. 1997. Kinetochore fiber maturation in PtK_1 cells and its implications for the mechanisms of chromosome congression and anaphase onset. *J. Cell Biol.* 137:1567–1580. http://dx.doi.org/10.1083/jcb.137.7.1567

Sundin, L.J., G.J. Guimaraes, and J.G. Deluca. 2011. The NDC80 complex proteins Nuf2 and Hec1 make distinct contributions to kinetochore-microtubule attachment in mitosis. *Mol. Biol. Cell*. 22:759–768. http://dx.doi.org/10.1091/mbc.E10-08-0671